Two-Path Neutrosophic Fully Convolutional Networks for Fluid Segmentation in Retina Images

B. Azimi[1], A.R. Rashno[*1], S. Fadaei[2]

[1] Department of Computer Engineering, Faculty of Engineering, Lorestan University, Khorramabad, Iran.
[2] Department of Electrical Engineering, Faculty of Engineering, Yasouj University, Yasouj, Iran.

ABSTRACT: Optical Coherence Tomography (OCT) images are used to reveal retinal diseases and abnormalities, such as Diabetic Macular Edema (DME) and Age-related Macular Degeneration (AMD). Fluid regions are the main sign of AMD and DME and automatic fluid segmentation models are very helpful for diagnosis, treatment, and follow-up. This paper presents a two-path Neutrosophic (NS) Fully Convolutional Networks, referred as TPNFCN, as a fully-automated model for fluid segmentation. For this task, OCT images are first transferred to NS domain and then Inner Limiting Membrane (ILM) and Retinal Pigmentation Epithelium (RPE) layers as first and last layers of retina are segmented by graph shortest path algorithms in NS domain, respectively. Afterwards, a basic block of FCN is presented for fluid segmentation and this block is used in the architecture of the proposed TPNFCN. Both the basic block and TPNFCN are evaluated on 600 OCT scans of 24 AMD subjects containing different fluid types. Results reveal that the proposed basic block and TPNFCN outperform five competitive models by improvement of 6.28%, 4.44% and 2.54% with respect to sensitivity, dice coefficients, and precision, respectively. It is also demonstrated that the proposed TPNFCN is robust against low number of training samples in comparison with current models.

1- Introduction

Ophthalmologists use retina images for diagnosis, follow-up, and treatment of retinal diseases. Fundus and Optical Coherence Tomography (OCT) are used as two technologies for retina imaging. Since there are many OCT images for each patient, it is very hard to segment fluid regions manually for all images by Ophthalmologists, and they run image processing algorithms and automated methods to segment fluid regions and extract other parameters such as blood vessels, layers, tissue, and optic disk of retina in each step of the treatment. Leakage of blood vessels leads to emerge fluid regions which is the most important sign of retina disease, such as Diabetic Macular Edema (DME) and Age-related Macular Degeneration (AMD). The volume of these regions is used for treatment and follow-up of DME and AMD.

Development of automated fluid segmentation models is the problem which is stated in this research. Regions underneath blood vessels, background and regions between retina layers are similar with fluid regions in color and texture. These regions are enumerated as main challenges for fluid segmentation problem. Deep learning models are successful in many applications. Fully Convolutional Network (FCN) as one of these models can be used for supervised pixel classification. For this task, each pixel in OCT images is labeled as fluid or tissue, and FCN can then be trained to predict the label pixels.

Neutrosophic (NS) sets are used to model data indeterminacy. Each data point is mapped to three sets, True (T), False (F) and Indeterminacy (I). In fluid segmentation, each pixel is mapped to T, I and F, means that it is T% true that this pixel is fluid, F% for tissue and the confident for this assignment is (1-I) %. In this research, NS is used to preprocess OCT images and subsequent steps are applied to images in NS domain. Based on explained methodologies to address OCT fluid segmentation challenges, main contributions of this research can be summarized as follows:

- OCT images are pre-processed by Region of Interest selection to avoid False Positive samples and speed up. For this task, first and last layers Internal Limiting Membrane (ILM) to the Retinal Pigment Epithelium (RPE) layers are segmented by a method based on graph shortest path and Neutrosophic sets.

- A basic model is proposed for fluid segmentation in Neutrosophic domain. In the proposed model, OCT scans are compressed to an arbitrary number of blocks and then decomposed to their original dimension to segment fluid regions.

- A Two-Path Neutrosophic Fully Convolutional Network (TPNFCN) is constructed from the basic model.

- Limitations and drawbacks of the proposed model are discussed in details.

Fluid segmentation methods have been presented in the literature based on image processing and machine learning

*Corresponding author's email: rashno.a@lu.ac.ir

methods. We proposed several fully-automated fluid segmentation methods for AMD and DME cases based on Convolutional Neural Networks (CNNs), Graph Cut, graph shortest path and Neutrosophic sets [1-8]. A challenge was done by Bogunovic, which was the most significant benchmark for fluid detection and segmentation [9]. NS has been applied in applications including image segmentation [10], content-based image retrieval [11, 12], choroid layer segmentation [4], fluid and cyst segmentation [1, 2, 5, 6, 8], correlation between initial vision and fluid regions [7], and skeletal muscle analysis [13].

In [14], deep neural networks were applied for fluid segmentation in OCT scan. A fluid and layer segmentation method based on Fully Convolutional Networks (FCNs), called as Relaynet, was presented in [15]. Retina thickness was segmented by CNNs in OCT scans [16]. Deep learning methods were used for automated detection and quantification of fluid in [17]. Another cystoid fluid quantification and detection relied on deep learning methods was presented in [18]. Generally, fluid regions can be segmented by pixel classification or image segmentation methods. In pixel classification, pixels are labeled based on color, shape, and texture features extracted from a window around each pixel [19, 20], while in image segmentation approaches, the whole image is segmented to a specific number of regions. In fluid segmentation application, pixels can be labeled as tissue or fluid, or the whole image can be segmented to fluid and tissue regions.

In [21], a new loss function named as Mutex Dice Loss is proposed by considering the priority of the mutex relationship between several layers. An FCN is introduced to segment three fluid types in OCT images in [22]. Two main steps of fluid segmentation were combined using direct modeling of the distribution of the surface locations in a unified CNN [23]. In [24], two intra-slice and inter-slice contrastive learning networks were designed separately and then combined to construct an end-to-end model for fluid segmentation. Another CNN with encoder and decoder blocks was presented in [25] to segment three lesion types of OCT images. In [26], a novel FCN scheme, including two segmentation and discrimination networks, was proposed to handle fluid segmentation in OCT images. A new approach named as LF-UNet was introduced in [27] to segment fluid in OCT images based on a double-branch CNNs. DenseNet was used to analyze the cystoid bodies in OCT images [28]. Automatic segmentation of fluid in OCT images was performed by an FCN approach in [29].

In [30], a semi-supervised framework based on combination of two teacher and student networks with similar structure was proposed. An attention-based network was presented in [31] to automatically localize fluid area by ignoring computational complexity of multi-stage approaches. Segmentation of different types of fluid in OCT images was applied to RETOUCH dataset using a deep neural network in [32]. In [33], a new FCN method named as DelNet was proposed to segment layers of retina in OCT images. Fluid segmentation

was done by introducing a fully-automated framework based on an FCN and graph shortest path in [34]. In [35], a deep neural network based on integration of Squeeze and Excitation referred as SE-UNet was presented for classification of OCT images as normal or AMD.

The rest of this paper is organized as follows: Section 2 presents the proposed method, including ROI Segmentation, basic model, and TPNFCN. Dataset is described in Section 3. Experimental setup and results are discussed in Sections 4 and 5, respectively. Limitations of the proposed FCN model are explained by examples in Section 6. Finally, this work is concluded in Section 7.

2- Proposed method
2- 1- Region of Interest Segmentation

In the first step, Region of Interest (ROI) is segmented as a region between Internal Limiting Membrane (ILM) to the Retinal Pigment Epithelium (RPE) layers [1]. This segmentation is very important since it eliminates background and reduces computational cost. For ROI segmentation, images are transferred to NS domain by Eqs. (1-5):

$$T(i,j) = \frac{\overline{g}(i,j) - \overline{g}_{\min}}{\overline{g}_{\max} - \overline{g}_{\min}} \tag{1}$$

$$F(i,j) = 1 - T(i,j) \tag{2}$$

$$I(i,j) = \frac{\delta(i,j) - \delta_{\min}}{\delta_{\max} - \delta_{\min}} \tag{3}$$

$$\overline{g}(i,j) = \frac{1}{\omega^2} \sum_{m=-\omega/2}^{\omega/2} \sum_{n=-\omega/2}^{\omega/2} g(i+m, j+n) \tag{4}$$

$$\delta(i,j) = |\overline{g}(i,j) - g(i,j)| \tag{5}$$

where $g, \overline{g}_{\min}, \overline{g}_{\max}$, T, I, and F represent gray level of input image, minimum gray level, maximum gray level, true, indeterminacy, and false sets, respectively. Afterwards, each pixel in image is mapped to one node of graph, and the edges between the nodes are computed from pixel gray-levels. For ILM segmentation, weights are calculated as follows:

$$VerGrad = T * H, H = \begin{bmatrix} -2 \\ 0 \\ +2 \end{bmatrix} \tag{6}$$
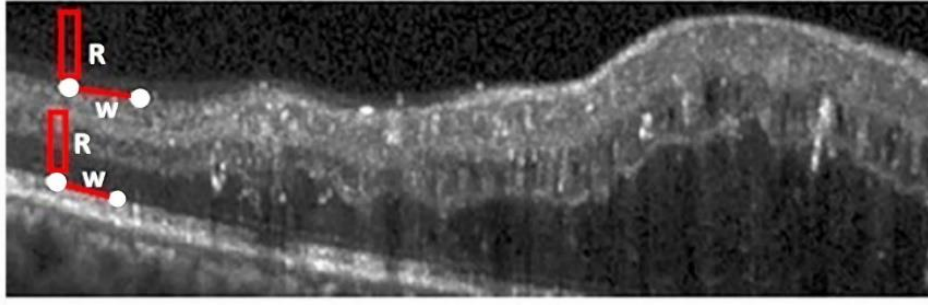
Fig. 1. Weight calculation for ILM and RPE segmentation.
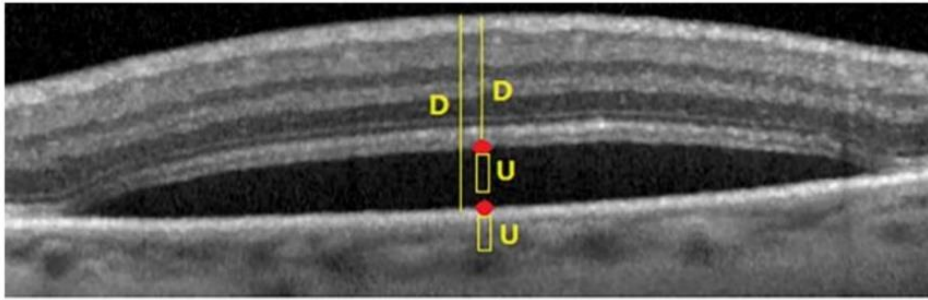
Fig. 2. Illustration of U and D.

$$W((a_1,b_1),(a_2,b_2)) = 4 \times MaxG - VerGrad(a_1,b_1) -$$

$$VerGrad(a_2,b_2) + 2 \times mean(R) \tag{7}$$

where R and *MaxG* are a vertical set of pixels above (a_1,b_1), and the maximum gradient in image, respectively. Fig. 1 illustrate R in the image. For RPE segmentation, as the last layer of the retinal, inverse of filter H pixels below (a_1,b_1) are considered [2]. For graph shortest path configuration, two nodes (pixels) up-left and down-right in OCT images are used as the start and end points, respectively. Finally, Dijkstra algorithm is used to select the shortest path between the start and end points. The shortest paths represent ILM and RPE, depending on the used filter [2].

Since fluid regions exist between ILM and RPE layers, no fluid region is lost in pre-processing in ROI segmentation. Additionally, due to the similarity between fluid regions and background, ROI segmentation improves accuracy of fluid segmentation methods. Finally, ROI segmentation leads to speeding up. Note that if the image does not contain the fluid, the weights can be calculated using Eq. (7), otherwise, Eq. (8) is used to construct weights:

$$W((a_1,b_1),(a_2,b_2)) = 4 \times MaxG - VerGrad(a_1,b_1) -$$

$$\cdot VerGrad(a_2,b_2) + 2 \times mean(U) - \beta D \tag{8}$$

where U is a vertical set of pixels below (a_1,b_1), D is the distance between (a_1,b_1), and the first layer of the network as illustrated in Fig. 2. β controls the importance of distance.

2- 2- Basic Block of the Proposed Model

The basic model structure is shown in Fig. 3 with two encoder and decoder parts. An OCT image with the size of 512×256×1, and a segmented ROI image with the size of 512×256×1 are concatenated to construct a two-channel image 512×256×2, which is considered as input of the network.

The encoder consists of four blocks and each block contains two convolution layers and one max-pooling. It is worth mentioning that after each convolution layer, ReLU activation function and batch normalization is applied. Each convolution layer of the first block has 32 filters with the size of 3×3. The size of max-pooling filter is 2×2 with stride 2 which creates the output image with a half of the input image. Therefore, output of the first block is 256×128×32. Note that before max-pooling layer, a copy of feature maps is saved to send to the corresponding block in the decoder section (skip connection). The next blocks are repeated the same way except that the number of filters in convolution layers are 64, 128, and 256 for blocks 2, 3, and 4, respectively.

After encoder, two convolution layers with 512 filters are applied to the output of the 4th block, which leads to the dimension of 16×32×512.
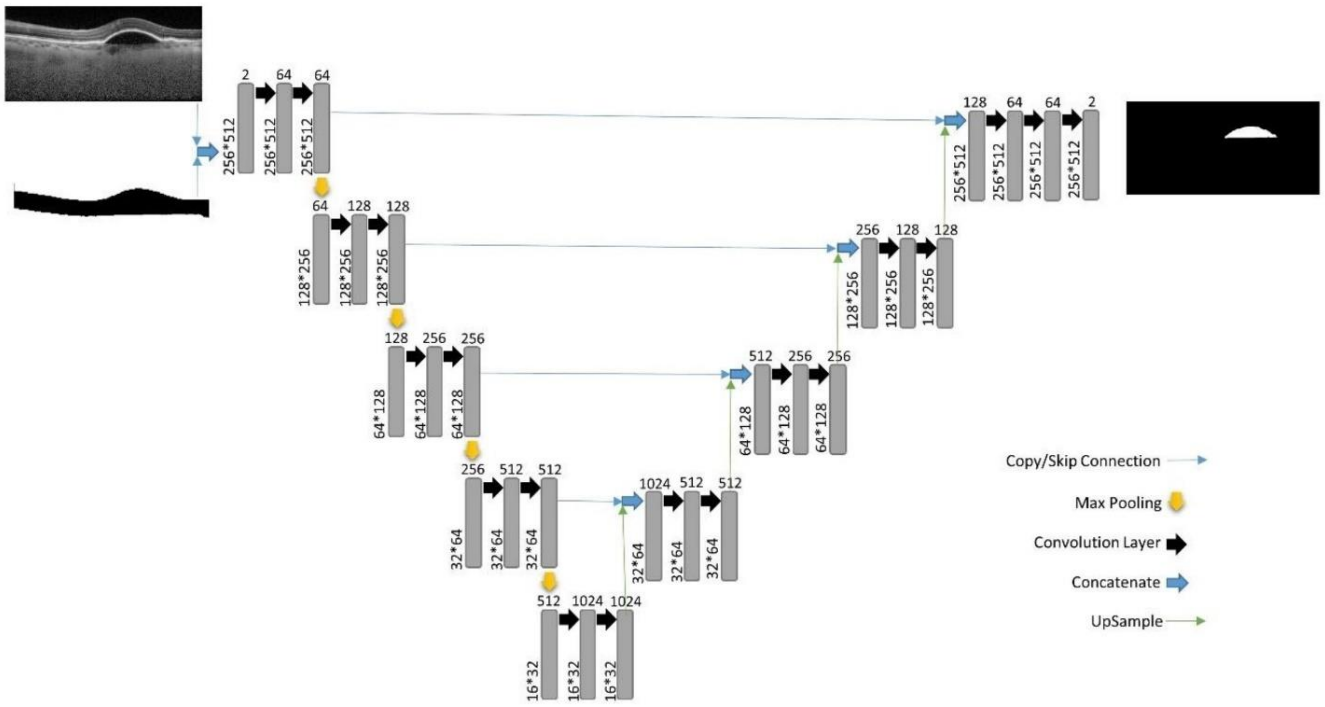
Fig. 3. Basic Block of the Proposed Model.

Data dimension is doubled by a transposed convolution operator in each block of decoder. Afterwards, the output of convolution layer in each level of the encoder is concatenated with the corresponding layer in the decoder as a skip connection. In the first step of decoder, channels of dimension 32×64×512 are created and two convolution layers with 256 filters and padding are applied, leading to the data size of 32×64×256. In blocks 2, 3, and 4, 128, 64 and 32 filters are considered, respectively. By applying consequent transposed convolution layers, we reach to the final dimension 256×512×32. Finally, since there are two classes of fluid and tissue for segmentation, 2 filters in a convolution layer are used to create final dimension 256×512×2.

2- 3- Architecture of the Proposed TPNFCN Model

Overfitting is the most important problem of FCNs which is due to low-dimension and noisy data. To avoid this problem, one solution is to use combination of models instead of one model. It is necessary to mention that although higher accuracy can be achieved by model combination, training time is increased significantly due to large number of parameters.

The proposed TPNFCN model is created based on the combination of two models, which make a great balance between accuracy and time complexity. Indeed, the input of each model is different and the outputs of the two models are concatenated. Fig. 4 shows the structure of the proposed TPNFCN. Since the proposed method is a two-path Neutrosophic FCN, it is referred as TPNFCN.

As shown in Fig. 4, the top model input is the OCT and ROI images, while the bottom model input is only the OCT image. It is important to note that in order to train the proposed structure, two models and the last convolution layer are considered as one network, not two distinct networks. In the top model, the size of OCT and ROI images are 512×256×1 and they are concatenated to construct an image with the size of 512×256×2. In the bottom model, the input image is an OCT image with the size of 512×256×1. The top and bottom models architecture are the same.

The encoder consists of 5 blocks, and each block contains 2 convolution layers and 1 max-pooling. ReLU activation function and batch normalization are applied after each convolution layer. In the first block, each convolution layer consists of 64 filters with the size of 3×3. Max-pooling layer size is 2×2 with stride 2, which its output size of is half of the input image size. Therefore, the size of the output image of the first block is 256×128×64. A copy of feature maps is saved and sent to the corresponding block in the decoder section before max-pooling layer (skip connection). The next blocks are repeated the same, except that the number of filters in convolution layers are 128, 256, 512, and 1024 for blocks 2, 3, 4, and 5, respectively. After the encoder steps, two convolution layers with 1024 filters are applied to the output of the 5th block which leads to the size of 8×16×2048.

In decoder, each level makes an up-sampling scheme by transposed convolution operator to create output size as twice as input size. This operation is equivalent with max-pooling
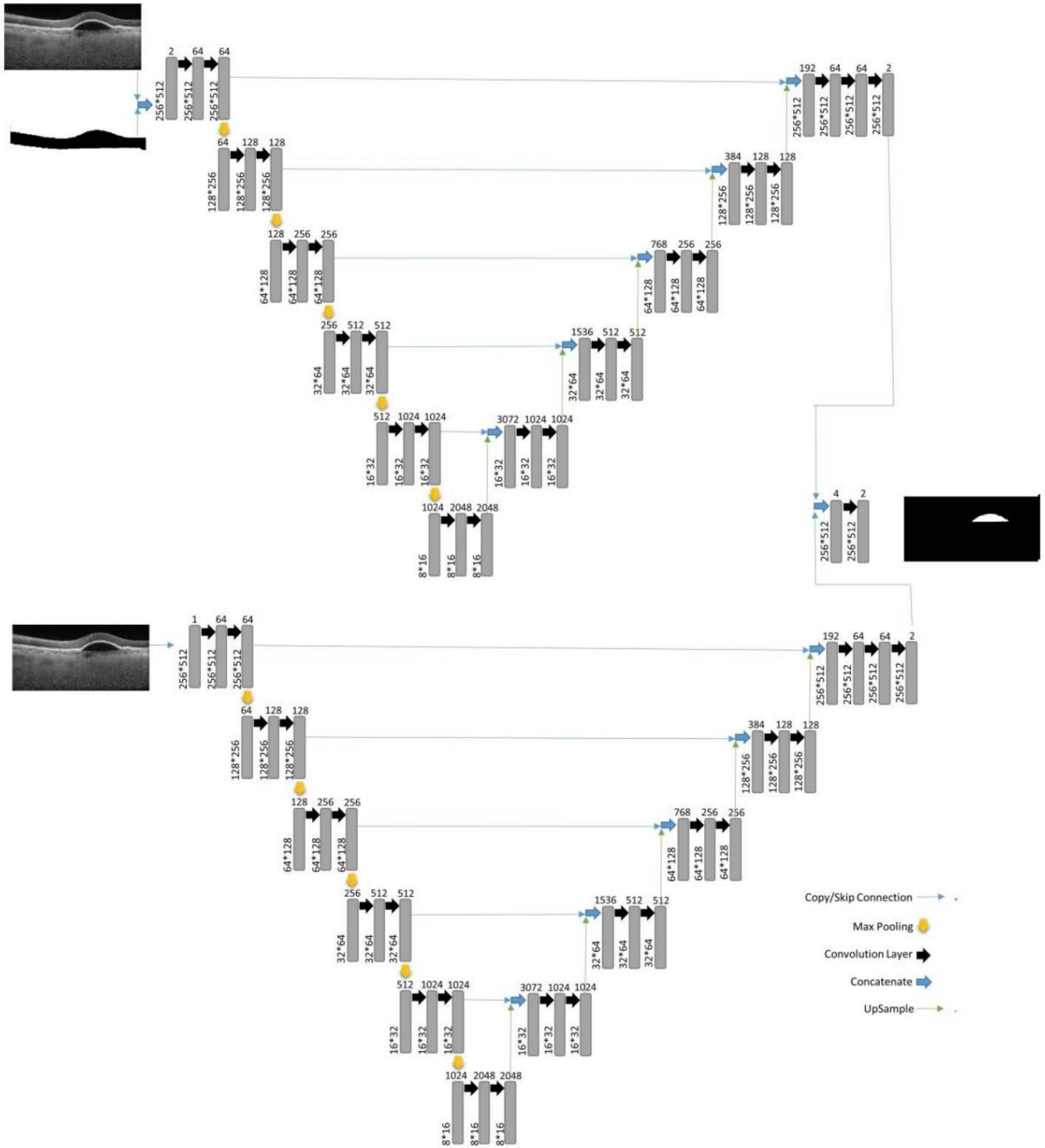
Fig. 4. Proposed TPNFCN for fluid segmentation.

inversion. Similar to the basic block, skip connections from decoder layers are used to make higher dimension outputs. In the first step, OCT channels of dimension 16×32×2048 are appeared and two 1024-filter convolution layers are used to make the dimension of 16×32×1024. In other decoder steps 2, 3, 4, and 5, filters 512, 256, 128, and 64 are used, respectively. Finally, transposed convolution operations used in each step make the final dimension of 256×512×64 in the encoder. To segment the OCT pixels as fluid or tissue, 2 filters are applied in the last convolution layer to reach the final dimension of 256×512×2. Note that this output is considered for each path of the proposed two-path FCN. It means that each path can segment fluid regions independently. By concatenation of outputs of two paths (top and bottom models), data with the dimension of 256×512×4 is generated. This data is further passed through a convolution layer with two filters which leads to 256×512×2 (2 channels), one channel is considered as fluid and another as tissue. Therefore, final fluid segmentation scheme can be achieved form the proposed model in Fig. 4.

3- OCT Dataset

The proposed TPNFCN model is assessed on a public OCT dataset of 24 subject, 25 scans per-subject, and 600 OCT images collected from the University of Minnesota. The dimension of each image is 496×1024. OCT scans have length and width direction resolutions in 5.88 and 3.87 μm/pixel, respectively. Fluid areas in all scans have been manually segmented by two ophthalmologists and used as ground truth images. All 600 images are divided into 141 and 459 scans for training and test, respectively. Among 141 images in the training phase, 58 scans are used for the training set and 83 for validation. In training set, intra-retinal, sub-RPE and subretinal are used to have all fluid types in FCN training.

4- Experimental Setup

To speed up the segmentation process, OCT images are resized to 256×512. Segmentation algorithm is applied to these images and then the segmented images are resized to their original size. All convolution layers convolve inputs by a kernel with the size of 3×3 continued by *LeakyReLu* activation function $(alpha = 0.2)$. The whole network is optimized by *cross entropy* loss function and *ADAM* optimizer. Note that there are two labels available for each pixel, one from expert 1 and another from expert 2. The proposed TPNFCN model is trained by labels from expert 1 and tested by two labels from expert 1 and 2. Finally, dice coefficient, sensitivity, and precision are computed from True Positive (TP), False Positive (TN), and False Negative (FN), and used as quantitative measures to evaluate segmentation performance:

$$\text{Sensitivity} = \frac{TP}{P} = \frac{TP}{TP + FN} \tag{9}$$

$$\text{Precision} = \frac{TP}{TP + FP} \tag{10}$$

$$\text{Dice Coefficiont} = 2 \times \frac{\text{Precision} \times \text{Sensitivity}}{\text{Precision} + \text{Sensitivity}} \tag{11}$$

5- Results

5- 1- Basic Block of the Proposed TPNFCN Results

In the first round of comparison, fluid regions segmented by basic block of the proposed TPNFCN are compared with Neutrosophic Graph Cut (NSGC) [2], Graph Cut (GC) [36], and Kernel Graph Cut (KGC) [37] methods in dice coefficient and sensitivity criteria. It is worth noting that the mentioned methods have been evaluated in OCT datasets used in this research. Two results are reported in each comparison, one between automated methods and expert 1, another with expert 2. Fig. 5 shows segmentation results of the proposed model in OCT scans containing fluid regions between retinal layers (intra-retinal fluid).

Other fluid types, sub-RPE and sub-retinal, are segmented by the proposed model in Figs. 6 and 7, respectively. The top image of Fig. 6 has 2 sub-PRE fluid regions, and in the other images, one region exists. The proposed TPNFCN model segments these fluid regions correctly. The same results are achieved in Fig. 7 as another samples for fluid segmentation.

Quantitative results of the basic block of the proposed TPNFCN and competitive models GC, KGC and NSGC in the term of dice coefficient are reported in Table 1.

Comparison between automated models and expert 1 and 2 are represented by E.1 and E.2, respectively. Based on the results in Table 1, it can be concluded that:

- The dice coefficient of the proposed Basic Block is maximum in subjects 1, 4-6, 8-13, 15-17 and 19-23 in comparison with E.1.
- Additionally, the Basic Block of the proposed TPNFCN outperforms other models in the terms of the dice coefficient in subjects 1-6, 8-15, 17, and 19-23, compared to E.2.
- NSGC is the best model in subjects 2, 3, 7, 14, 18, and 24 compared to E.1 and 7, 16, 18, and 24 compared to E.2.
- The Basic Block of the proposed TPNFCN has the highest average dice coefficient 86.00% compared to NSGC (81.56%), KGC (65.25%) and GC (69.13%).
- The best dice coefficient is achieved by the Basic Block and is 96.45% (subject 23) and 95.54% (subject 8) compared to E.1 and E.2, respectively.

Sensitivity measure of all methods are reported in Table 2 as another quantitative measure. It can be concluded that:

- For sensitivity measure, the Basic Block of the proposed TPNFCN is the best model in subjects 1, 3-6, 8-17, 19, and 21-24 in E.1 comparison.
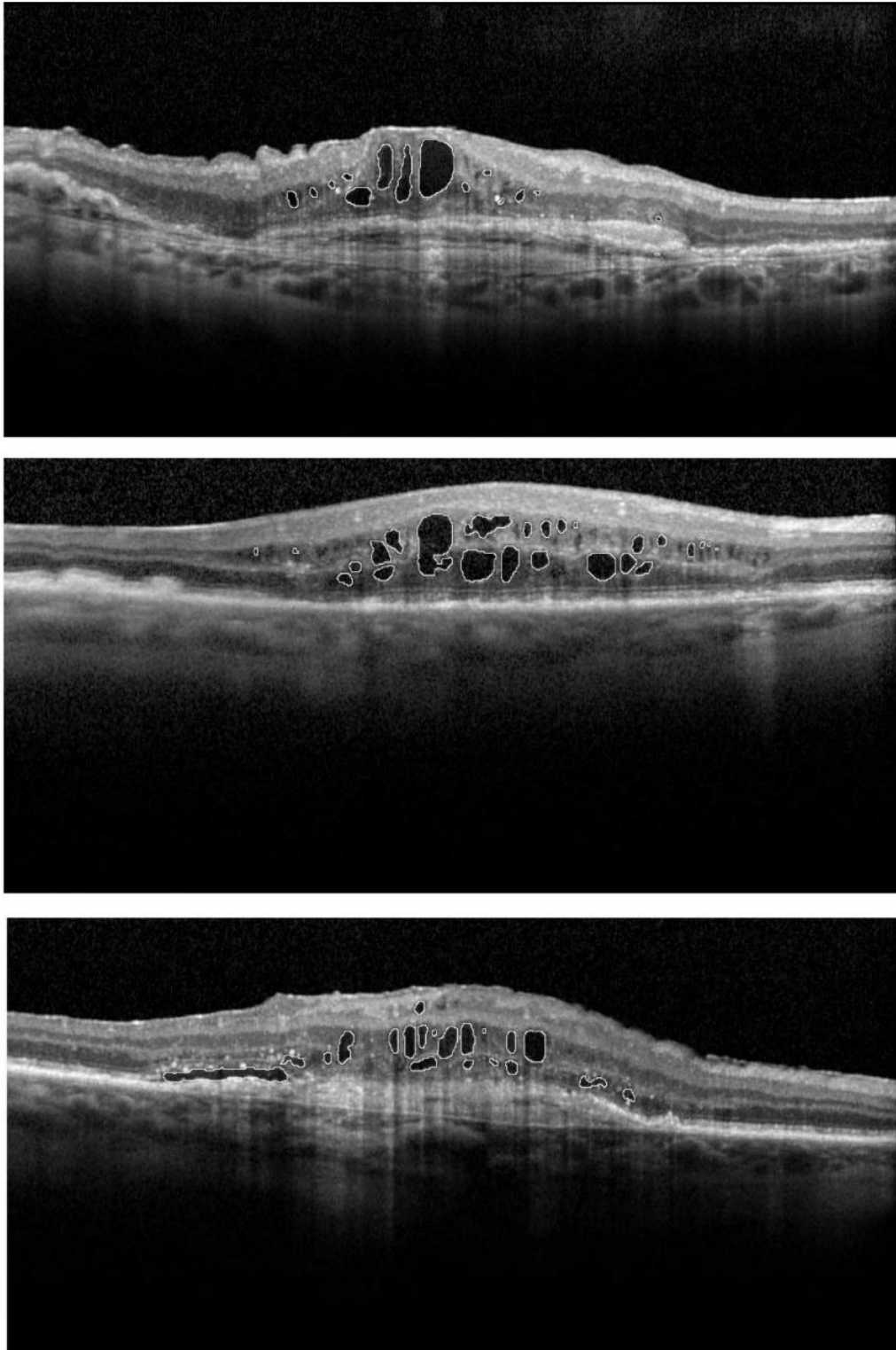
Fig. 5. Segmentation results of basic block of the proposed TPNFCN in OCT scans containing intra-retinal fluid.
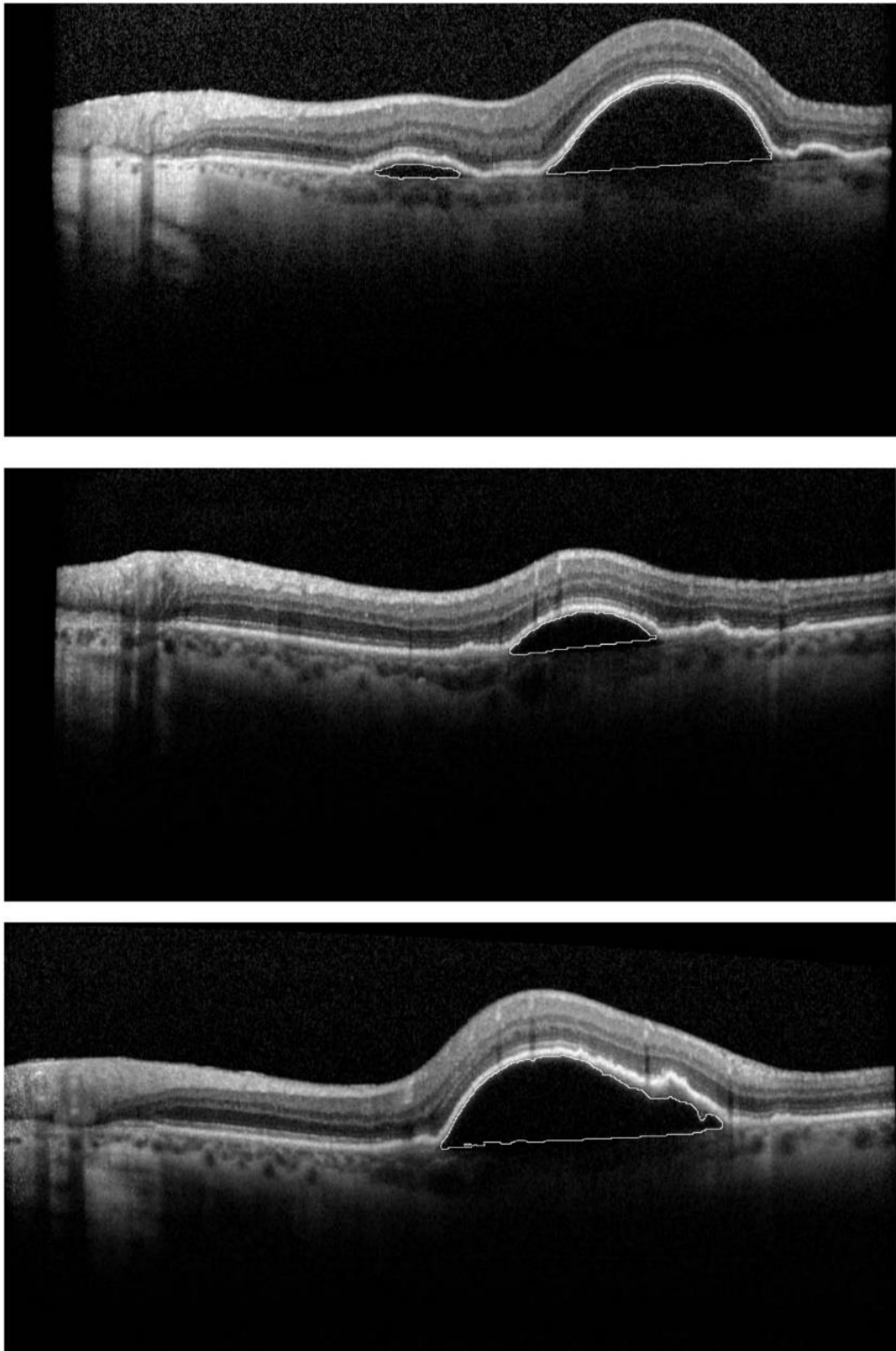
Fig. 6. Segmentation results of the basic block of the proposed TPNFCN in OCT scans containing sub-RPE fluid.
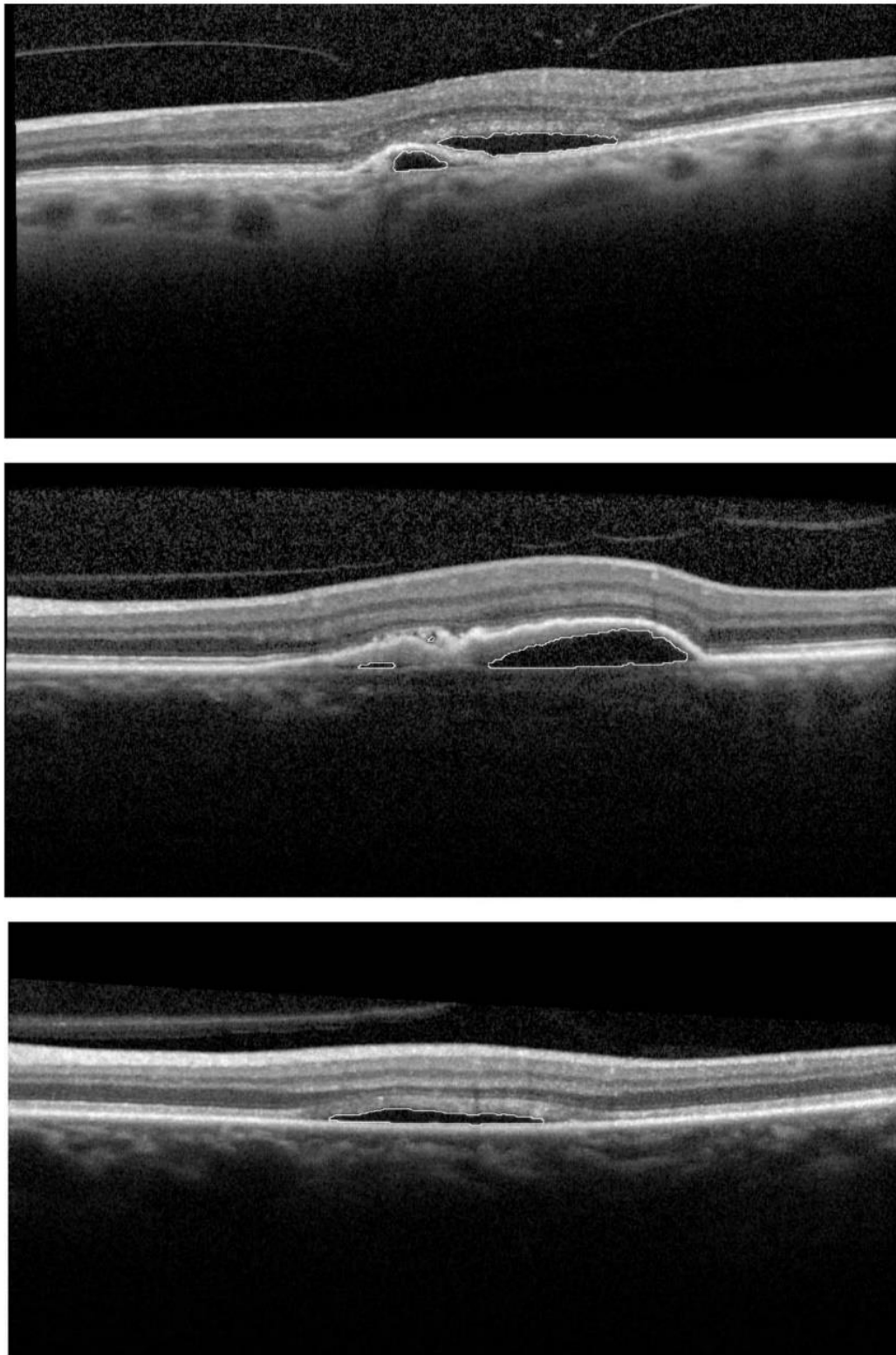
Fig. 7. Segmentation results of the basic block of the proposed TPNFCN in OCT scans containing sub-retinal fluid.

Table 1. Dice coefficient results of all methods.

Sub.	Dice coefficient							
	GC		KGC		NSGC		Basic Block of the Proposed TPNFCN	
	E.1	E.2	E.1	E.2	E.1	E.2	E.1	E.2
1	78.68	75.34	79.07	74.76	85.68	81.81	**94.41**	**94.84**
2	77.79	77.83	86.11	82.03	**89.49**	85.36	89.19	**91.78**
3	56.54	53.05	56.56	51.91	**85.81**	79.40	84.87	**83.75**
4	71.94	72.26	69.51	69.49	82.81	82.34	**84.45**	**83.60**
5	45.80	43.70	25.20	24.64	68.25	66.02	**75.80**	**72.82**
6	73.32	68.61	61.34	57.10	85.91	80.53	**93.92**	**94.08**
7	56.71	52.61	46.32	42.00	**67.31**	**63.13**	54.84	58.04
8	86.89	86.25	79.06	79.07	86.85	86.29	**95.79**	**95.54**
9	76.65	72.61	74.95	70.92	83.00	78.81	**95.33**	**95.24**
10	76.54	76.39	76.57	76.44	84.63	80.51	**90.01**	**89.81**
11	72.22	67.74	55.28	51.02	86.51	82.26	**92.42**	**87.17**
12	71.34	68.03	69.53	66.08	82.42	79.43	**90.41**	**85.87**
13	62.61	62.57	64.67	64.56	89.90	89.85	**92.28**	**92.19**
14	63.48	59.26	57.34	53.47	**81.07**	76.98	78.23	**78.19**
15	61.94	53.73	58.19	50.26	74.16	66.07	**78.74**	**76.48**
16	71.17	71.07	69.21	69.20	87.62	**87.57**	**91.76**	85.89
17	73.03	72.17	88.31	83.58	91.52	86.48	**92.16**	**91.45**
18	66.27	58.43	66.93	59.49	**84.70**	**77.06**	76.90	74.66
19	73.93	73.64	43.31	43.26	86.38	82.09	**90.54**	**85.94**
20	65.76	57.41	69.75	63.05	85.40	75.13	**85.64**	**79.79**
21	81.11	70.62	76.04	66.16	89.00	78.38	**93.27**	**83.03**
22	71.33	64.40	61.50	55.00	77.16	70.19	**82.13**	**82.08**
23	89.83	79.47	90.85	82.49	91.68	82.66	**96.45**	**87.67**
24	81.37	77.12	87.27	83.22	**88.79**	**84.77**	88.44	83.37
Ave	71.01	67.26	67.20	63.30	84.00	79.13	**87.29**	**84.72**
Ave	69.13		65.25		81.56		**86.00**	

- The Basic Block of the proposed TPNFCN is the best model in all subjects in E.2 comparison.
- In subjects 2, 7, 18, and 20, NSGC reaches the best sensitivity in E.1 comparison.
- The proposed Basic Block achieves the best sensitivity score in both E.1 (97.29% in subject 8) and E.2 (96.73% in subject 1).
- Generally, the Basic Block of the proposed TPNFCN with the sensitivity of 87.38% outperforms NSGC (81.10%), KGC (75.69%), and GC (70.11%).

It reveals that the proposed Basic Block achieves the best results quantitively and qualitatively. Therefore, this block is used in the final FCN model.

5- 2- The Proposed TPNFCN Model Results

The proposed TPNFCN model is compared with two models, UNet and SE-UNet. Note that the proposed TPNFCN is not compared to GC, KGC, and NSGC, since these models were compared to Basic Block of TPNFCN, and TPNFCN has better results that Basic Block. Fig. 8 shows the segmentation results of TPNFCN, UNet, and SE-UNet applied to 9 samples of OCT images. In this figure, column **a** represents OCT samples and columns **b**, **c** and **d** show the segmentation results of UNet, SE-UNet, and the proposed TPNFCN, respectively. It is obvious that the proposed model segments fluid regions more carefully than the other models.

In experiments, 3 (train,test) sets (58,542), (200,400), and (375,225) are considered as sets 1, 2, and 3, respectively. Table 3 reports Dice coefficient, Sensitivity, and Precision of TPNCNN and other methods in set 1. In each row, the maximum value is shown in bold format.

Results in Table 3 can be concluded as:
- SE-UNet achieves the improvements of 1.58%, 1.62%, and 1.04% in dice coefficient, sensitivity, and precision, respectively, compared to UNet. The reason is that SE-

Table 2. Sensitivity of the basic block of the proposed TPNFCN and other methods.

Sub.	Sensitivity							
	GC		KGC		NSGC		Basic Block of the Proposed TPNFCN	
	E.1	E.2	E.1	E.2	E.1	E.2	E.1	E.2
1	74.39	71.24	83.03	79.40	84.38	81.01	**96.55**	**96.73**
2	84.24	80.33	92.42	88.31	**94.38**	90.36	90.74	**93.79**
3	50.70	47.26	67.23	62.30	81.82	75.08	**86.04**	**85.23**
4	61.70	62.15	79.60	79.88	84.92	84.89	**86.91**	**86.67**
5	56.10	53.13	54.73	53.18	67.90	64.26	**77.84**	**73.76**
6	81.38	76.73	78.80	74.62	87.78	82.34	**96.98**	**96.25**
7	57.14	54.03	56.70	52.05	**66.37**	63.28	60.50	**64.02**
8	88.43	87.18	86.39	86.14	92.75	91.56	**97.29**	**96.64**
9	79.37	75.32	78.24	74.30	89.31	84.95	**96.19**	**96.10**
10	74.39	70.24	77.86	73.59	82.91	78.44	**91.96**	**91.77**
11	74.29	69.78	77.00	72.63	82.23	77.62	**94.51**	**88.92**
12	62.61	59.60	67.56	64.88	77.15	74.84	**91.28**	**87.45**
13	76.83	76.96	84.06	84.02	88.31	88.13	**92.38**	**92.39**
14	62.24	57.92	65.87	61.82	78.27	73.80	**80.38**	**80.64**
15	64.41	56.20	66.02	57.76	74.24	66.04	**79.39**	**77.20**
16	88.08	84.04	88.63	84.69	90.34	86.29	**92.17**	**86.43**
17	79.57	74.88	89.29	84.13	90.71	85.36	**96.56**	**95.22**
18	59.55	51.68	67.45	59.86	**81.33**	73.30	79.02	**77.82**
19	72.30	67.93	77.73	73.44	83.24	78.57	**91.55**	**87.10**
20	75.35	62.68	87.05	74.09	**88.61**	75.60	86.02	**79.85**
21	77.60	64.02	84.37	69.73	85.61	69.97	**94.84**	**80.33**
22	83.81	73.53	90.66	78.71	87.94	76.80	**91.51**	**79.23**
23	85.90	73.21	94.24	79.51	87.77	72.97	**96.75**	**82.09**
24	74.72	70.33	86.72	82.41	86.85	82.57	**88.21**	**83.04**
Ave	72.71	67.52	78.40	72.98	83.96	78.25	**88.98**	**85.78**
Ave	70.11		75.69		81.10		**87.38**	

UNet uses feature map weighting.

• The proposed TPNFCN improves UNet by 3.84%, 4.16%, and 2.54% in dice coefficient, sensitivity, and precision, respectively. It also improves SE-UNet results by 2.26%, 2.54%, and 1.50% in the same measures.

• The proposed TPNFCN is the best method in 16 subjects out of 24 ones in dice coefficient, 18 subjects out of 24 ones in sensitivity, and 9 subjects out of 24 ones in precision. It is worth mentioning that the SE-UNet is better than the TPNFCN model in 13 subjects.

Dice coefficient, Sensitivity, and Precision for set 2 have been reported in Table. 4. It can be concluded that:

• TPNFCN outperforms UNet and SE-UNet by 1.70% and 0.45% in dice coefficient, and 2.49% and 1.46% in sensitivity, respectively.

• In the term of dice coefficient, SE-UNet achieves a better performance of 1.11% and 0.79% in comparison with UNet and TPNFCN.

• The proposed TPNFCN is the best method in 18 subjects out of 24 ones in dice coefficient, 17 subjects out of 24 ones in sensitivity.

• SE-UNet is better than other methods in 13 subjects out of 24 in precision.

Table 5 reports the results of 375 and 225 training sets. In this experiment:

• SE-Unet achieves improvement of 1.22% and 3.04% in dice coefficient and sensitivity in comparison with Unet, respectively.

• The proposed TPNFCN improves Unet and SE-Unet by 1.47% and 0.25% in dice coefficient and 3.40% and 0.36% in sensitivity, respectively.

• Unet is the best method in comparison with other methods in precision criterion and improves SE-Unet and TPNFCN by 1.19% and 1.09%, respectively.

• The proposed TPNFCN is the best method in 13 subjects out of 24 ones in dice coefficient and 12 subjects out of 24 ones in sensitivity. Unet is better than others in 20 subjects out of 24 in precision.

(a) (b) (c) (d)
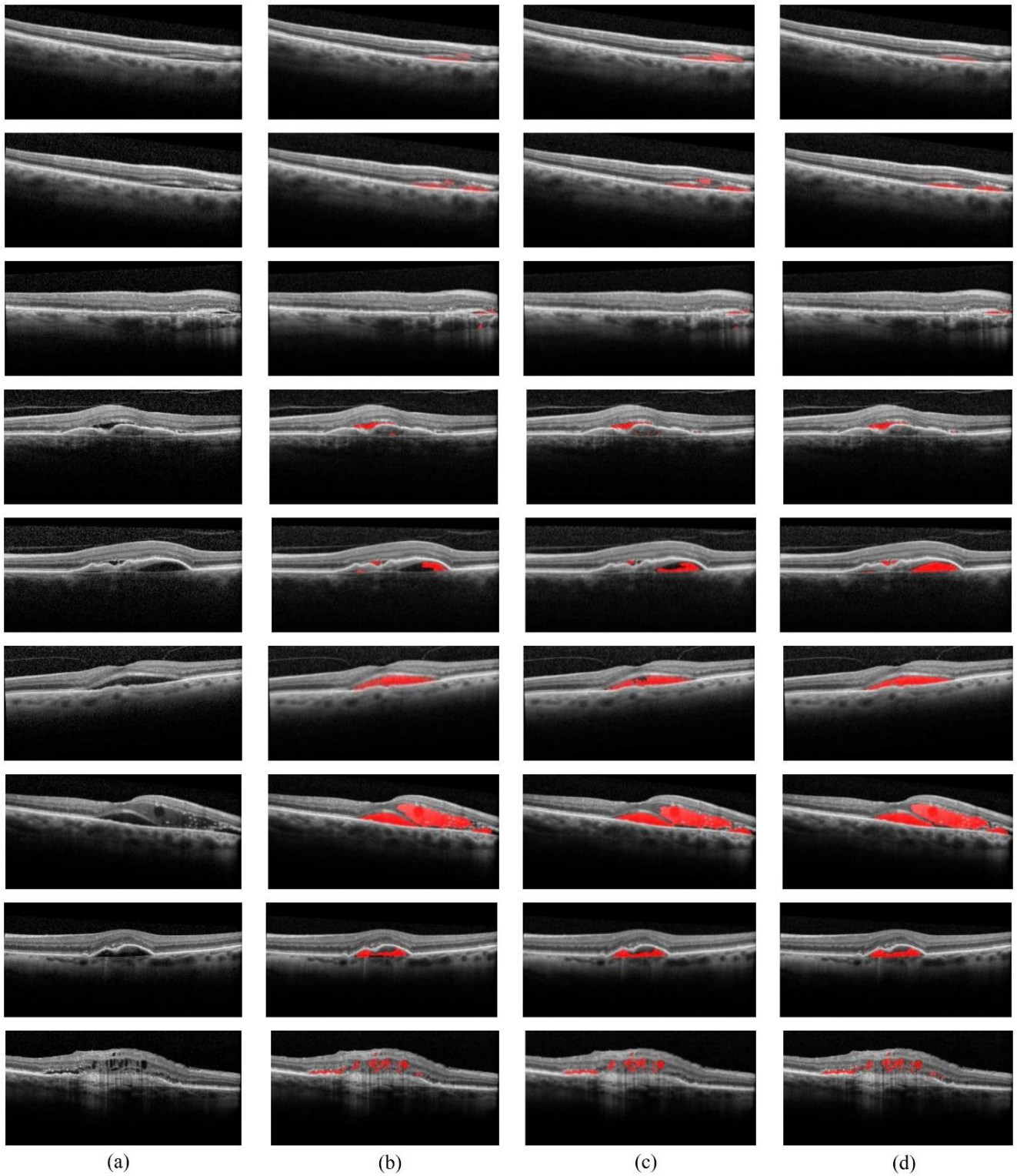
Fig. 8. Fluid segmentation results of OCT samples (column a), Column b: UNet; Column c: SE-UNet; Column d: TPNFCN.

Table 3. Dice coefficient, Sensitivity and Precision of TPNCNN and other methods in set 1.

	58 training images and 542 test images								
Patient	**Dice coefficient**			**Sensitivity**			**Precision**		
	UNet	**SE-UNet**	**TPNFCN**	**UNet**	**SE-UNet**	**TPNFCN**	**UNet**	**SE-UNet**	**TPNFCN**
1	94.66	94.23	**94.97**	91.72	90.93	**92.51**	98.00	**98.07**	97.67
2	**90.23**	90.03	89.01	**87.54**	86.20	86.62	93.42	**94.69**	91.86
3	97.58	**97.84**	97.74	95.72	**96.11**	96.00	99.80	**99.88**	99.79
4	76.27	81.88	**89.43**	71.16	80.46	**85.35**	82.78	87.43	**94.49**
5	66.52	60.83	**76.20**	56.88	51.14	**68.94**	88.08	77.69	**88.14**
6	70.69	67.24	**72.12**	**67.11**	66.77	65.04	78.28	71.48	**83.84**
7	68.65	79.05	**79.41**	65.30	**75.54**	75.20	80.71	83.95	**85.51**
8	90.28	91.30	**91.45**	89.35	88.09	**89.36**	91.84	**95.03**	93.81
9	**96.07**	96.04	95.83	94.09	93.94	**94.18**	98.32	**98.46**	97.67
10	**97.42**	96.66	96.93	**95.92**	95.22	95.33	**99.09**	98.26	98.72
11	95.37	95.37	**95.74**	92.68	92.58	**93.70**	98.67	**98.84**	98.10
12	87.87	87.58	**89.67**	79.63	79.01	**82.38**	98.49	**98.71**	98.54
13	93.57	**94.42**	93.91	89.57	**90.78**	90.19	98.52	**98.81**	98.41
14	72.28	73.39	**92.20**	68.87	68.44	**88.15**	78.79	83.22	**97.20**
15	83.41	88.84	**88.95**	79.42	84.38	**84.97**	94.54	**96.56**	95.66
16	**93.37**	93.33	93.22	88.60	88.64	**88.66**	**98.93**	98.77	98.50
17	89.82	**91.11**	90.89	88.60	89.46	**91.82**	91.55	**93.09**	90.91
18	87.25	88.84	**89.40**	81.53	83.00	**83.89**	94.82	**96.60**	**96.60**
19	85.22	86.75	**87.71**	79.50	81.93	**84.10**	**95.68**	94.75	94.91
20	74.33	94.07	**95.48**	71.56	91.04	**92.93**	78.84	**99.40**	99.28
21	95.85	95.22	**96.50**	93.62	91.99	**94.22**	98.21	98.70	**98.91**
22	96.37	96.05	**97.53**	93.89	95.29	**95.88**	99.07	96.87	**99.28**
23	94.45	95.45	**96.26**	93.45	95.07	**96.02**	95.68	96.07	**96.66**
24	**95.15**	95.12	94.35	94.29	92.83	**94.34**	96.15	**97.68**	94.59
Average	87.20	88.78	**91.04**	83.75	85.37	**87.91**	92.84	93.88	**95.38**

5- 3- Discussion
5- 3- 1- Challenges and Limitations of Comparisons

The basic block is the core of the proposed model. It has been compared to GC, KGC and NSKGC with a constant number of training samples. The main reason for this comparison is to show the effectiveness of the basic block. When the basic block is used to construct more advanced model TPNFCN, it has been compared to UNet and SE-UNet with the different number of training samples. Note that in SE-UNet, data augmentation is used to generate sufficient training data, since in this model 450 OCT images are not abundant to train the model. Random translation, reflection, rotation, flipping, and cropping are used to increase training samples to reach 13500 OCT images. In the proposed model, data augmentation is not applied to the training samples and the model is trained with a few numbers of samples which is

a light-weight model. This advantage is discussed in details in the third case of results analysis in the next section. It is worth mentioning that increasing the number of training samples improves the performance of the model. Therefore, training models without data augmentation is not in conflict with fair comparison between models.

5- 3- 2- Conclusions of Experiments

- UNet does not have successful segmentation in low number of training samples. It fails to detect True Positives, which leads to low performance in Sensitivity measure. By increasing the training samples, UNet is improved and its results are close to other models (even reaches to the best Precision). It means that UNet is very sensitive to the number of training samples.

Table 4. Dice coefficient, Sensitivity and Precision of TPNCNN and other methods in set 2.

Patient	200 training images and 400 test images								
	Dice coefficient			Sensitivity			Precision		
	UNet	SE-Unet	TPNFCN	Unet	SE-Unet	TPNFCN	Unet	SE-Unet	TPNFCN
1	94.66	94.63	**95.06**	91.20	91.53	**92.92**	**98.72**	98.20	97.41
2	90.12	89.78	**90.30**	87.66	86.44	**89.69**	93.04	**93.77**	90.99
3	97.94	98.15	**98.41**	96.22	96.67	**97.20**	**99.98**	99.85	99.75
4	88.02	88.50	**89.20**	81.27	82.01	**85.36**	**97.39**	96.97	94.07
5	75.03	**78.64**	76.13	65.96	**70.78**	67.37	**91.71**	90.51	90.76
6	76.32	79.13	**79.84**	**74.39**	71.36	74.32	80.31	**89.91**	88.47
7	63.43	65.01	**68.23**	64.91	59.71	**65.27**	65.54	**73.98**	71.92
8	91.82	92.40	**93.01**	89.24	89.87	**92.11**	94.71	**95.22**	93.96
9	96.07	95.72	**96.66**	94.36	93.91	**96.34**	**97.98**	97.76	97.00
10	96.82	96.44	**97.22**	95.35	94.13	**96.59**	98.46	**99.17**	97.88
11	95.89	95.09	**96.16**	93.31	92.62	**94.18**	**99.03**	98.10	98.47
12	88.77	89.91	**90.75**	80.74	**85.59**	84.66	**98.75**	94.84	97.89
13	94.68	93.94	**95.40**	91.33	89.96	**93.14**	98.69	**98.86**	97.92
14	78.52	92.23	**93.34**	74.65	87.33	**90.34**	83.36	**98.69**	96.90
15	90.86	89.89	**90.98**	86.51	86.07	**86.82**	98.19	96.13	**98.59**
16	93.54	93.69	**94.36**	89.11	89.08	**92.12**	98.65	**99.02**	96.80
17	92.62	92.86	**93.48**	90.34	90.32	**92.65**	95.42	**95.81**	94.47
18	88.73	89.51	**90.03**	83.52	**86.41**	85.16	95.39	93.95	**96.91**
19	83.23	**89.68**	88.12	77.26	84.71	**85.00**	96.16	**97.22**	93.99
20	95.12	94.86	**95.99**	92.46	91.98	**94.66**	99.23	**99.57**	97.57
21	96.61	**97.13**	96.74	94.63	**96.04**	95.85	**98.68**	98.26	97.71
22	96.87	**97.89**	97.44	95.33	**96.45**	95.77	98.55	**99.43**	99.23
23	96.20	**96.38**	95.92	96.79	**98.59**	97.01	**95.83**	94.44	95.10
24	95.34	**95.68**	95.06	94.24	94.03	**95.99**	96.59	**97.50**	94.22
Average	89.88	91.13	**91.58**	86.70	87.73	**89.19**	94.60	**95.71**	94.92

- SE-UNet improves its performance in Sensitivity measure when its training samples is increased. This method is less sensitive to the number of training samples compared to UNet.

- The best property of the proposed TPNFCN is its robustness against low number of training samples. It has acceptable results in all cases of sets (training, test). It is clear from the reported results that the best improvement of TPNFCN is achieved in the lowest number of training samples.

- The performance of all methods is close to each other when the majority of samples is used for training samples (set 3).

-

6- Discussion and Challenges of TPNFCN

Some challenges of OCT images affect segmentation accuracy of all automated models. In this section, these chal-

lenges are discussed.

6- 1- Challenge of ROI Segmentation

The first issue is inaccurate ROI segmentation. Since the fluid regions inside ROI are considered for segmentation, any fluid region out of ROI is ignored. Therefore, error in ROI segmentation leads to error in fluid segmentation, especially in cases that fluid regions are close to ILM and RPE. An example of this case is illustrated in Fig. 9. Fluid region underneath RPE is ignored since RPE is segmented incorrectly.

6- 2- Challenge of Dark Non-Fluid Regions

Some non-fluid regions are similar to fluid regions in color and texture. This issue is revealed in cases containing sub-retinal fluid. In these cases, non-fluid regions are located above fluid regions and misleads TPNFCN as shown in Fig. 10.

Table 5. Dice coefficient, Sensitivity and Precision of TPNCNN and other methods in set 3.

Patient	Dice coefficient			Sensitivity			Precision		
	Unet	SE-Unet	TPNFCN	Unet	SE-Unet	TPNFCN	Unet	SE-Unet	TPNFCN
1	94.16	95.15	**95.17**	90.14	**92.51**	92.41	**98.99**	98.11	98.26
2	89.03	89.92	**90.55**	85.05	**88.90**	88.37	**93.95**	91.24	93.08
3	97.48	**98.14**	98.13	95.43	**96.60**	96.56	**99.99**	99.92	99.94
4	88.64	89.75	**89.97**	81.11	**85.04**	84.46	**98.82**	95.36	96.96
5	72.72	76.51	**78.79**	61.74	**74.56**	71.30	**95.42**	81.10	90.59
6	77.16	**81.10**	80.55	66.36	75.03	**76.41**	92.63	89.42	86.97
7	79.38	79.47	**80.38**	76.59	75.56	76.58	83.40	**97.24**	85.48
8	91.66	91.38	**93.03**	87.55	90.04	**90.59**	96.52	93.08	95.71
9	95.62	96.04	**96.42**	93.09	95.03	**95.16**	98.61	97.13	97.80
10	95.86	96.97	**97.01**	93.52	**95.52**	95.43	98.66	98.58	**98.77**
11	95.42	96.06	**96.30**	92.30	93.85	**94.31**	99.41	98.67	98.62
12	88.71	**92.03**	90.36	80.56	**86.93**	83.50	**98.85**	97.85	98.62
13	94.54	**95.62**	95.53	90.65	92.88	**93.11**	99.33	98.73	98.27
14	92.25	**93.36**	93.33	87.50	**89.75**	89.51	**98.51**	97.69	98.08
15	90.15	90.13	**91.32**	86.07	87.20	**88.17**	96.93	94.64	95.76
16	92.71	**94.30**	94.14	87.08	**90.40**	90.10	**99.48**	98.72	98.74
17	91.68	92.93	**93.14**	88.14	**90.96**	90.88	**96.00**	95.24	95.79
18	89.31	**91.38**	90.57	82.68	**87.97**	85.92	**98.77**	95.52	96.34
19	88.17	90.11	**92.06**	81.93	85.38	**88.50**	**98.35**	96.34	96.27
20	94.54	94.98	**95.48**	91.58	92.33	**93.01**	**99.53**	99.07	99.09
21	96.16	**96.80**	96.73	92.83	94.31	**94.49**	**99.82**	99.47	99.09
22	96.88	**97.39**	97.29	94.35	95.48	**95.55**	**99.69**	99.49	99.18
23	96.12	**97.18**	97.18	95.17	96.84	**97.17**	97.23	**97.57**	97.29
24	95.17	**96.09**	95.33	93.13	94.58	**95.17**	97.49	**97.71**	95.62
Average	90.98	92.20	**92.45**	86.44	89.48	**89.84**	**97.35**	96.16	96.26

6- 3- Challenge of Undesired Artifacts

TPNFCN is triggered by dark regions similar to fluids. Issues in imaging process including instrument problems, nonuniform illumination, retinal movement, and noise make artifacts in OCT images. These undesired artifacts create dark regions without layer structure and are good candidates to be incorrectly segmented as fluid regions (Fig. 11).

6- 4- Challenge of Elevated RPE and Blood Vessels

Some non-fluid regions named as drusen are created from Elevated RPE. TPNFCN wrongly segments these regions as fluid. Such errors can be decreased if the RPE layer is segmented more accurately. Another dark region is revealed underneath blood vessels since blood absorbs light and creates such regions. These regions are also segmented as fluid while they are not. Samples of these cases are demonstrated in Fig. 12.

6- 5- Challenge of Small Fluid Regions Under RPE

Very small fluid regions under RPE are ignored by many fluid segmentation models, as shown in Fig. 13. It is due to inaccurate RPE segmentation and their low distance from choroid. Furthermore, dark regions alongside retina layers are wrongly segmented as fluid. This error can be controlled by middle layers segmentation.

7- Conclusion

Optical Coherence Tomography (OCT) images are used to reveal retinal diseases and abnormalities, such as Diabetic Macular Edema (DME) and Age-related Macular Degeneration (AMD). Fluid regions are the main sign of AMD and DME, and automatic fluid segmentation models are very helpful for diagnosis, treatment, and follow-up. A Fully Convolutional Network with two paths in Neutrosophic (NS) domain was presented in this work, called TPNFCN. In the first
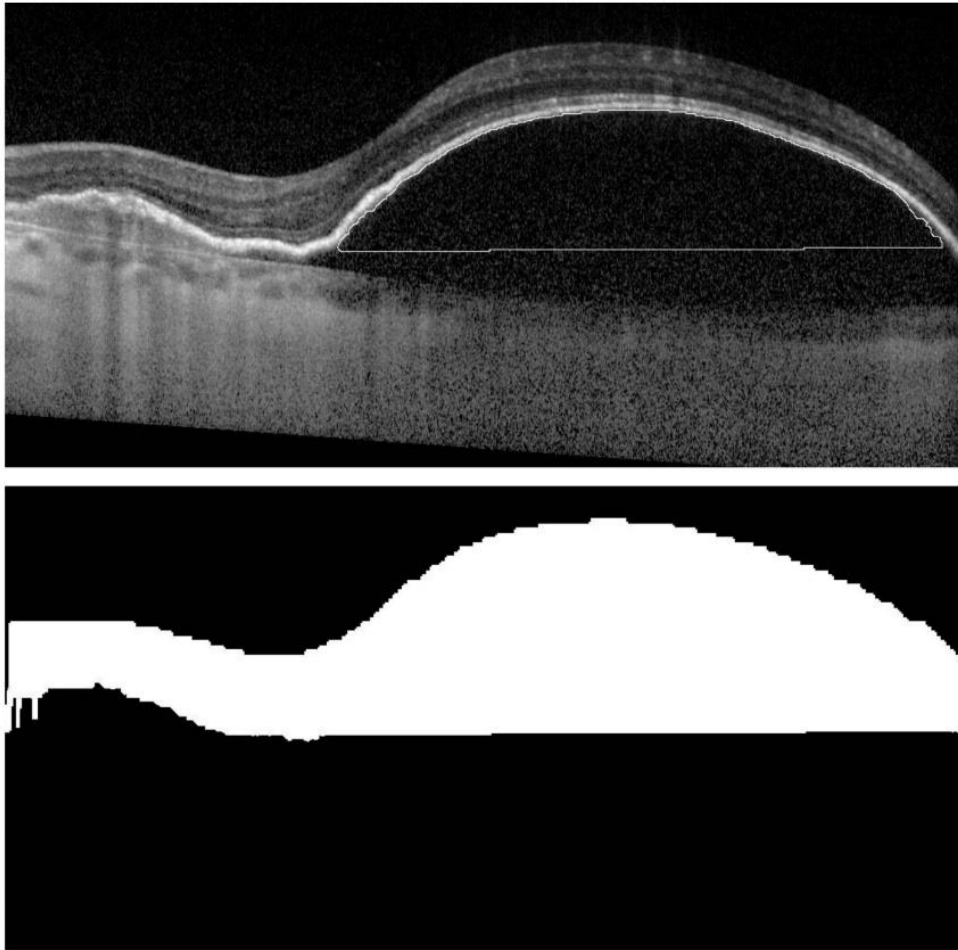
Fig. 9. Fluid segmentation error stems from RPE segmentation error.
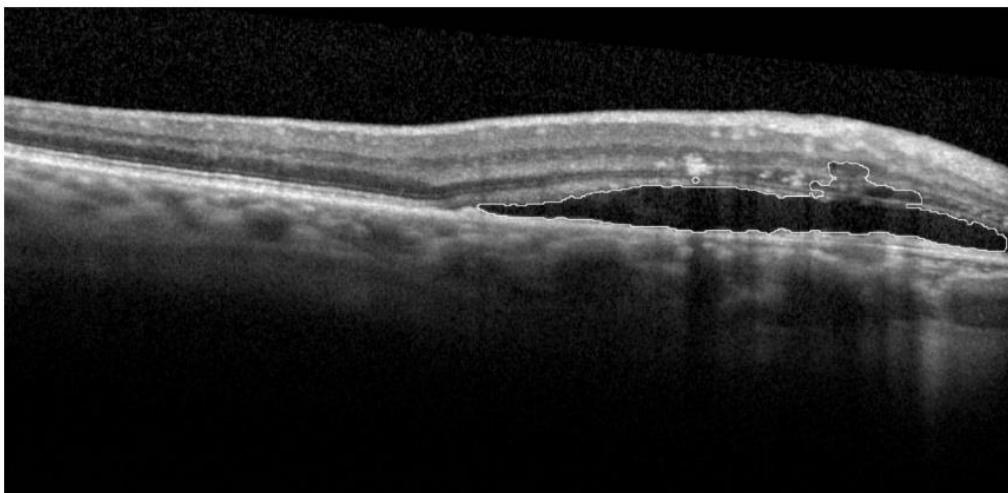
Fig. 10. Fluid segmentation errors stem from non-fluid dark regions.
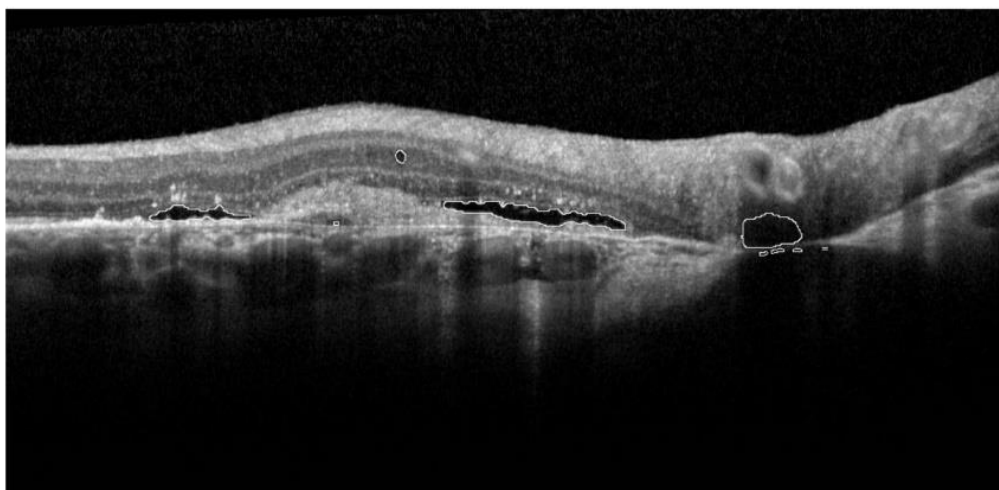
Fig. 11. Fluid segmentation errors stem from undesired artifacts.
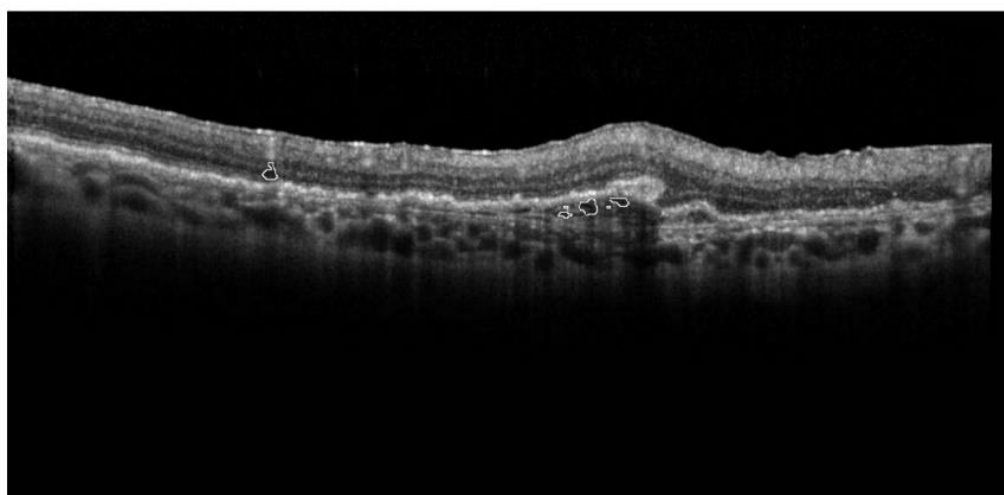
Fig. 12. Fluid segmentation errors stem from elevated RPE.

step, Inner Limiting Membrane (ILM) and Retinal Pigmentation Epithelium (RPE) layers are segmented by graph shortest path as first and last layers of retina, respectively. Next, a basic FCN block is presented for fluid segmentation and is used in the architecture of the proposed TPNFCN. Both the basic block and TPNFCN are evaluated on 600 OCT scans of 24 AMD subjects containing different fluid types. Results reveal that the proposed basic block and TPNFCN outperforms 5 competitive models by improvement of 6.28%, 4.44%, and 2.54% with respect to sensitivity, dice coefficients, and precision, respectively. It is also demonstrated that the proposed TPNFCN is robust against low number of training samples in comparison with current models.

References

[1] A. Rashno, D.D. Koozekanani, P.M. Drayna, B. Nazari, S. Sadri, H. Rabbani, K.K. Parhi, Fully automated segmentation of fluid/cyst regions in Optical Coherence Tomography images with Diabetic Macular Edema using Neutrosophic sets and graph algorithms, IEEE Transactions on Biomedical Engineering, 65(5) (2017) 989-1001.

[2] A. Rashno, B. Nazari, D.D. Koozekanani, P.M. Drayna, S. Sadri, H. Rabbani, K.K. Parhi, Fully-automated segmentation of fluid regions in exudative Age-related Macular Degeneration subjects: Kernel Graph Cut in Neutrosophic domain, PloS one, 12(10) (2017) e0186949.

[3] A. Rashno, D.D. Koozekanani, K.K. Parhi, Oct fluid

segmentation using graph shortest path and Convolutional Neural Network, in: 2018 40th Annual International Conference of the IEEE Engineering in Medicine and Biology Society (EMBC), IEEE, 2018, pp. 3426-3429.

[4] B. Salafian, R. Kafieh, A. Rashno, M. Pourazizi, S. Sadri, Automatic segmentation of choroid layer in edi oct images using graph theory in Neutrosophic space, arXiv preprint arXiv:1812.01989, (2018).

[5] A. Rashno, K.K. Parhi, B. Nazari, S. Sadri, H. Rabbani, P. Drayna, D.D. Koozekanani, Automated intra-retinal, sub-retinal and sub-rpe cyst regions segmentation in Age-related Macular Degeneration (amd) subjects, Investigative Ophthalmology & Visual Science, 58(8) (2017) 397-397.

[6] K.K. Parhi, A. Rashno, B. Nazari, S. Sadri, H. Rabbani, P. Drayna, D.D. Koozekanani, Automated fluid/cyst segmentation: A quantitative assessment of Diabetic Macular Edema, Investigative Ophthalmology & Visual Science, 58(8) (2017) 4633-4633.

[7] J. Kohler, A. Rashno, K.K. Parhi, P. Drayna, S. Radwan, D.D. Koozekanani, Correlation between initial vision and vision improvement with automatically calculated retinal cyst volume in treated dme after resolution, Investigative Ophthalmology & Visual Science, 58(8) (2017) 953-953.

[8] E. Rashno, A. Rashno, S. Fadaei, Fluid segmentation in Neutrosophic domain, in: 2019 5th Iranian Conference on Signal Processing and Intelligent Systems (ICSPIS), IEEE, 2019, pp. 1-5.

[9] H. Bogunović, F. Venhuizen, S. Klimscha, S. Apostolopoulos, A. Bab-Hadiashar, U. Bagci, M.F. Beg, L. Bekalo, Q. Chen, C. Ciller, RETOUCH: the retinal OCT fluid detection and segmentation benchmark and challenge, IEEE transactions on medical imaging, 38(8) (2019) 1858-1874.

[10] A. Heshmati, M. Gholami, A. Rashno, Scheme for unsupervised colour–texture image segmentation using Neutrosophic set and non-subsampled contourlet transform, IET Image Processing, 10(6) (2016) 464-473.

[11] A. Rashno, S. Sadri, Content-based image retrieval with color and texture features in Neutrosophic domain, in: 2017 3rd International Conference on Pattern Recognition and Image Analysis (IPRIA), IEEE, 2017, pp. 50-55.

[12] A. Rashno, F. Smarandache, S. Sadri, Refined Neutrosophic sets in content-based image retrieval application, in: 2017 10th Iranian Conference on Machine Vision and Image Processing (MVIP), IEEE, 2017, pp. 197-202.

[13] M. Rahmati, A. Rashno, Automated image segmentation method to analyse skeletal muscle cross section in exercise-induced regenerating myofibers, Scientific reports, 11(1) (2021) 1-16.

[14] S.H. Kang, H.S. Park, J. Jang, K. Jeon, Deep neural networks for the detection and segmentation of the retinal fluid in OCT images, MICCAI Retinal OCT Fluid Challenge (RETOUCH), (2017).

[15] A.G. Roy, S. Conjeti, S.P.K. Karri, D. Sheet, A. Katouzian, C. Wachinger, N. Navab, ReLayNet: retinal layer and fluid segmentation of macular Optical

Coherence Tomography using Fully Convolutional Network s, Biomedical optics express, 8(8) (2017) 3627-3642.

[16] F.G. Venhuizen, B. van Ginneken, B. Liefers, M.J. van Grinsven, S. Fauser, C. Hoyng, T. Theelen, C.I. Sánchez, Robust total retina thickness segmentation in Optical Coherence Tomography images using Convolutional Neural Networks, Biomedical optics express, 8(7) (2017) 3292-3316.

[17] T. Schlegl, S.M. Waldstein, H. Bogunovic, F. Endstraßer, A. Sadeghipour, A.-M. Philip, D. Podkowinski, B.S. Gerendas, G. Langs, U. Schmidt-Erfurth, Fully automated detection and quantification of macular fluid in OCT using deep learning, Ophthalmology, 125(4) (2018) 549-558.

[18]] F.G. Venhuizen, B. van Ginneken, B. Liefers, F. van Asten, V. Schreur, S. Fauser, C. Hoyng, T. Theelen, C.I. Sánchez, Deep learning approach for the detection and quantification of intraretinal cystoid fluid in multivendor Optical Coherence Tomography, Biomedical optics express, 9(4) (2018) 1545-1569.

[19] A. Rashno, S. Sadri, H. SadeghianNejad, An efficient content-based image retrieval with ant colony optimization feature selection schema based on wavelet and color features, in: 2015 The International Symposium on Artificial Intelligence and Signal Processing (AISP), IEEE, 2015, pp. 59-64.

[20] A. Rashno, B. Nazari, S. Sadri, M. Saraee, Effective pixel classification of mars images based on ant colony optimization feature selection and extreme learning machine, Neurocomputing, 226 (2017) 66-79.

[21] H. Wei, P. Peng, The segmentation of retinal layer and fluid in SD-OCT images using mutex dice loss based Fully Convolutional Networks, IEEE Access, 8 (2020) 60929-60939.

[22] G. Xing, L. Chen, H. Wang, J. Zhang, D. Sun, F. Xu, J. Lei, X. Xu, Multi-scale pathological fluid segmentation in OCT with a novel curvature loss in Convolutional Neural Network, IEEE Transactions on Medical Imaging, (2022).

[23] Y. He, A. Carass, Y. Liu, B.M. Jedynak, S.D. Solomon, S. Saidha, P.A. Calabresi, J.L. Prince, Structured layer surface segmentation for retina OCT using fully convolutional regression networks, Medical image analysis, 68 (2021) 101856.

[24] X. He, L. Fang, M. Tan, X. Chen, Intra-and Inter-Slice Contrastive Learning for Point Supervised OCT Fluid Segmentation, IEEE Transactions on Image Processing, (2022).

[25] R. Tennakoon, A.K. Gostar, R. Hoseinnezhad, A. Bab-Hadiashar, Retinal fluid segmentation in OCT images using adversarial loss based Convolutional Neural Networks, in: 2018 IEEE 15th International Symposium on Biomedical Imaging (ISBI 2018), IEEE, 2018, pp. 1436-1440.

[26] X. Liu, T. Fu, Z. Pan, D. Liu, W. Hu, B. Li, Semi-supervised automatic layer and fluid region segmentation of retinal Optical Coherence Tomography images using adversarial learning, in: 2018 25th IEEE International

Conference on Image Processing (ICIP), IEEE, 2018, pp. 2780-2784.

[27] D. Ma, D. Lu, S. Chen, M. Heisler, S. Dabiri, S. Lee, H. Lee, G.W. Ding, M.V. Sarunic, M.F. Beg, LF-UNet–A novel anatomical-aware dual-branch cascaded deep neural network for segmentation of retinal layers and fluid from Optical Coherence Tomography images, Computerized Medical Imaging and Graphics, 94 (2021) 101988.

[28] P.L. Vidal, J. de Moura, J. Novo, M. Ortega, Cystoid fluid color map generation in Optical Coherence Tomography images using a densely connected Convolutional Neural Network, in: 2019 International Joint Conference on Neural Networks (IJCNN), IEEE, 2019, pp. 1-8.

[29] T.N. Rao, G. Girish, A.R. Kothari, J. Rajan, Deep learning based sub-retinal fluid segmentation in central serous chorioretinopathy Optical Coherence Tomography scans, in: 2019 41st Annual International Conference of the IEEE Engineering in Medicine and Biology Society (EMBC), IEEE, 2019, pp. 978-981.

[30] X. Liu, S. Wang, Uncertainty-Aware Semi-Supervised Framework for Automatic Segmentation of Macular Edema in Oct Images, in: 2021 IEEE 18th International Symposium on Biomedical Imaging (ISBI), IEEE, 2021, pp. 1453-1456.

[31] X. Liu, S. Wang, Y. Zhang, D. Liu, W. Hu, Automatic fluid segmentation in retinal Optical Coherence Tomography images using attention based deep learning, Neurocomputing, 452 (2021) 576-591.

[32] K. Alsaih, M. Yusoff, T. Tang, I. Faye, F. Mériaudeau, Retinal Fluids Segmentation Using Volumetric Deep Neural Networks on Optical Coherence Tomography Scans, in: 2020 10th IEEE International Conference on Control System, Computing and Engineering (ICCSCE), IEEE, 2020, pp. 68-72.

[33] B. Anoop, R. Pavan, G. Girish, A.R. Kothari, J. Rajan, Stack generalized deep ensemble learning for retinal layer segmentation in Optical Coherence Tomography images, Biocybernetics and Biomedical Engineering, 40(4) (2020) 1343-1358.

[34] B. Azimi, A. Rashno, S. Fadaei, Fully Convolutional Networks for Fluid Segmentation in Retina Images, in: 2020 International Conference on Machine Vision and Image Processing (MVIP), IEEE, 2020, pp. 1-7.

[35] Z. Chen, D. Li, H. Shen, H. Mo, Z. Zeng, H. Wei, Automated segmentation of fluid regions in Optical Coherence Tomography B-scan images of Age-related Macular Degeneration, Optics & Laser Technology, 122 (2020) 105830.

[36] Y. Boykov, G. Funka-Lea, Graph Cuts and efficient ND image segmentation, International journal of computer vision, 70(2) (2006) 109-131.

[37] M.B. Salah, A. Mitiche, I.B. Ayed, Multiregion image segmentation by parametric Kernel Graph Cuts, IEEE Transactions on Image Processing, 20(2) (2010) 545-557.